

# Convective intensification of solar surface magnetic fields: results of numerical experiments

U. Grossmann-Doerth, M. Schüssler, and O. Steiner

Kiepenheuer-Institut für Sonnenphysik, Schöneckstr. 6, D-79104 Freiburg, Germany  
 (ugd@kis.uni-freiburg.de; msch@kis.uni-freiburg.de; steiner@kis.uni-freiburg.de)

Received 27 February 1998 / Accepted 3 June 1998

**Abstract.** The concentration of magnetic flux by convective flows in the solar surface layers is studied by means of two-dimensional numerical simulations with radiative transfer. We follow the evolution of an initially homogeneous, vertical magnetic field, starting from an evolved state of simulated solar granulation. The results of three simulation runs with initial field strengths,  $B_0$ , of 100 G, 200 G, and 400 G, respectively, are shown. In all cases, horizontal convective flows rapidly sweep magnetic flux into the intergranular downflow channels. The field is further amplified up to kilogauss values by partial evacuation due to a strongly accelerated downflow within the magnetic structure. The value of the field strength reached at a given depth and the size of the flux concentrations grows with the initial field strength (i.e., the amount of magnetic flux within the computational box). In the case of  $B_0 = 400$  G, the downflow within the flux concentration becomes so strong that it ‘bounces’ off the high density plasma in the deeper layers; the resulting upflow leads to a strong, upward moving shock and to the dispersal of the flux sheet after a lifetime of about 200 s. In the cases with less magnetic flux ( $B_0 = 100$  G, 200 G), the downflow is less vigorous and the flux concentrations persist to the end of the simulation (about 5 minutes). Radiation diagnostics in the continuum and in spectral lines predicts observable signatures of the intensification process. The accelerated downflow leads to a conspicuous Doppler shift and a negative area asymmetry of Stokes  $V$ -profiles of spectral lines, while the intensification of the magnetic field may be detectable through the ‘magnetic line ratio’ method in the visible and by direct Zeeman splitting of magnetically sensitive lines in the infrared wavelength ranges.

**Key words:** Sun: magnetic fields – Sun: photosphere – Sun: atmosphere – Sun: granulation – Sun: faculae, plages – MHD

## 1. Introduction

What are the physical processes that lead to the intermittent distribution of small-scale kilogauss magnetic fields observed in the solar photosphere (e.g., Solanki 1993)? ‘Flux expulsion’ in cellular convective flows (Parker 1963, Weiss 1966) prob-

ably explains the observed concentration of the magnetic flux at the edges of granular and supergranular cells. Under solar conditions, however, this kinematical effect alone is not able to increase the field strength significantly above the equipartition value of about 500 G (Parker 1979). The Lorentz force suppresses further growth of the field by impeding the horizontal flow, unless large turbulent diffusivities with a magnetic Prandtl number significantly exceeding unity are invoked (Galloway et al. 1977).

It is widely believed that further amplification of the magnetic field strength is due to *thermal* effects. Since the horizontal flows of granular convection carry heat to the downflow regions, the retardation of the flows by the growing magnetic field leads to an enhanced cooling of the magnetic region because the radiative losses cannot be balanced by the reduced horizontal flow. The cooling and the strongly superadiabatic stratification of the uppermost layers of the convection zone accelerate the downflow along the field lines (Parker 1978) and, since the horizontal flow is suppressed by the Lorentz force, a partial evacuation of the upper layers ensues. Pressure equilibrium with the surrounding gas is restored by compression of the flux tube, increasing the magnetic pressure. In this way, the magnetic field can be locally intensified to values which are only limited by the confining pressure of the external gas.

Within the framework of the thin-flux-tube approximation, this process has been studied by means of linear stability analysis (Webb & Roberts 1978, Spruit & Zweibel 1979, Unno & Ando 1979) and through numerical calculations (Venkatakrisnan 1983, 1985, 1986; Hasan 1984, 1985). Starting from a static state with temperature equilibrium between a vertical flux tube and the surrounding superadiabatically stratified atmosphere, linear analysis predicts instability if the initial field strength is sufficiently small. This instability manifests itself either as an accelerated downflow with gas pressure reduction and increase of the field strength (‘convective collapse’) or as an accelerated upflow leading to pressure enhancement and magnetic field dispersal. Depending on the boundary conditions, the depth of the flux tube, the adopted model atmosphere, and the initial value of  $\beta \equiv 8\pi p_{\text{gas}}/B^2$ , a stable state can be reached if the field strength has grown so large that  $\beta \lesssim 2$  (Spruit 1979). Non-linear, time-dependent calculations of the instability, still in the thin-tube limit, either lead to (overstable) oscillations or to a

final static state depending on whether the lower boundary is closed or open for the fluid flow (Takeuchi 1993, 1995). Nordlund (1986, see also Nordlund & Stein 1989) finds evidence for convective intensification in three-dimensional simulations of solar magneto-convection, although the spatial resolution in these calculations is not sufficient for a detailed study of small-scale magnetic features.

Here we present results of numerical experiments in two spatial dimensions. The restriction to 2D enables us to achieve relatively high spatial resolution at affordable computational cost while retaining the essential ingredients of the intensification process. At the same time, we allow for internal structure and dynamics of the developing flux concentrations and obtain spectroscopic information that may be compared with observations. The two-dimensionality of the numerical model may seem more restrictive than it actually is since elongated magnetic structures form in intergranular lanes when magnetic flux is squashed between two granules. It is conceivable that such flux sheets show a much stronger variation in the direction perpendicular to the lane than parallel to it, so that a two-dimensional model appears not too unrealistic.

## 2. Numerical model

We solve the full set of the time-dependent MHD equations, including the effects of (grey) radiative transfer and hydrogen ionization, within a two-dimensional rectangular spatial domain. The direction of the  $x$ -coordinate is parallel to the solar surface, spanning a distance of 2400 km. The  $y$ -coordinate runs 1400 km in the vertical (height) direction, ranging from 800 km below the surface (optical depth unity at 500 nm for a mean solar atmosphere model) to 600 km above it. We use a uniform rectangular grid with  $240 \times 140$  node points, so that a cell size of  $10 \times 10 \text{ km}^2$  results. The equations are written in conservation law form and are discretized according to the Flux-Corrected Transport (FCT) algorithm (see, e.g., Oran & Boris 1987). The effect of turbulent eddies smaller than the grid resolution is taken into account by using sub-grid-scale (SGS) diffusivities, following the approach of Chan & Sofia (1986). Details about the code and tests are described in Steiner et al. (1994); previous simulation results based on this code can be found in Steiner et al. (1996, 1998).

The horizontal boundary conditions are periodic. At the top we prescribe a vanishing temperature gradient since this boundary coincides with the temperature minimum region; in this optically thin layer, the energy transported by radiation is nearly independent of the local temperature gradient. The vertical velocities are damped within an ‘absorbing layer’ (Sato & Hayashi 1979) of 100 km thickness in order to suppress the (unphysical) reflection of waves and shocks. The lower boundary permits free in- and outflow of gas. We prescribe a constant total pressure,  $p_T = p_{\text{gas}} + B^2/8\pi$ , along this boundary (thus assuming instantaneous horizontal balance of total pressure at the bottom) and adjust this value so that the total mass within the computational domain remains constant in time. The entropy of the inflowing gas is specified in such a way that the time-averaged radiation

output at the top of the computational domain corresponds to the mean solar value. The magnetic field lines are vertical at the top and bottom boundaries; they are free to move in the horizontal direction.

The numerical implementation of an open or wave-absorbing boundary condition in a stratified medium is a problem that has not yet been generally solved (see, e.g., Nordlund & Stein 1990, Hossain & Mullan 1993, Nordlund et al. 1994). In the simulations discussed here we focus on processes taking place in layers that have a much larger density than the tenuous region near the top boundary. Therefore, the results are probably not strongly affected by the precise formulation of the upper boundary condition.

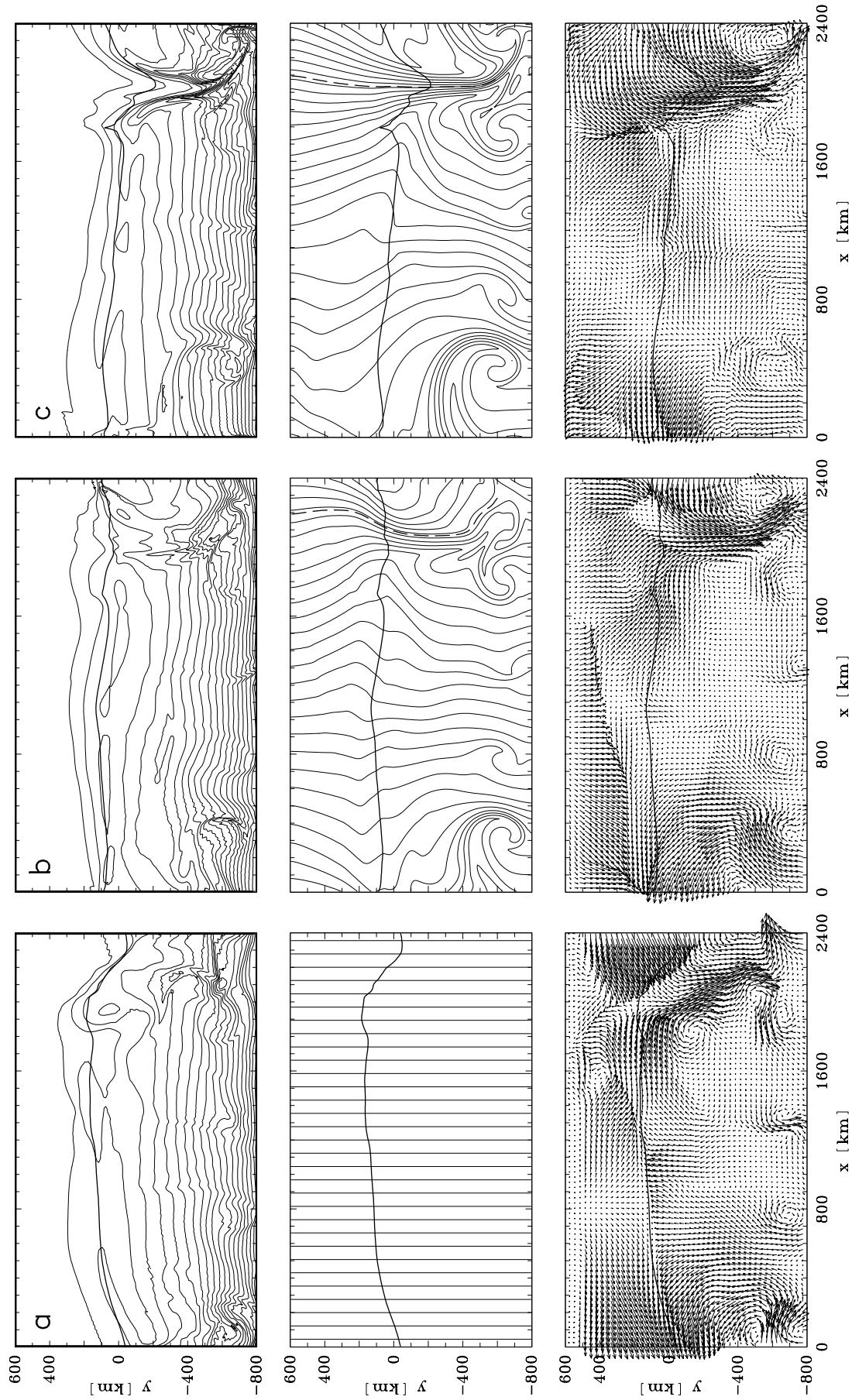
The numerical experiments are carried out in the following way. We begin with the simulation of a field-free plasma, starting with a plane-parallel stratification taken from the model of Spruit (1977). We perturb this convectively unstable configuration by a velocity field of small amplitude and let the system evolve until it relaxes to a ‘normal’ pattern of instationary convective motion. We then impose a homogeneous, vertical magnetic field onto the entire computational domain and follow the ensuing interaction between the magnetic field and the convective motions.

## 3. Simulation results

We have performed three simulation runs, which differ by the strength of the initial magnetic field and in the pattern of convection at the time when the magnetic field is imposed. Run C1 has an initial field of 100 G, run C4 starts from the same convective pattern, but with a field of 400 G, while run C2 starts from a different pattern and has an initial field of 200 G.

We first describe the results of run C4. Fig. 1a–e displays the time evolution, showing (from top to bottom) density contours, magnetic field lines, and the velocity field at five moments corresponding to 0, 50, 100, 150, and 250 seconds, respectively, after the introduction of the magnetic field. In the last snapshot (e) isotherms are shown in the top panel instead of density contour lines. The level of continuum (500 nm) optical depth unity is indicated in all panels by a thick, solid line.

In the beginning we have an extended upflow covering a large part of the computational domain. Downflowing gas is concentrated in a narrow channel (at  $x \simeq 2000 \text{ km}$ ) of roughly 200 km width. Magnetic flux is rapidly swept to this channel by the horizontal flow and forms a flux concentration, which becomes visible in snapshot (b). Between instants (b) and (d) the downflow within the magnetic field is accelerated to up to  $12 \text{ km s}^{-1}$  peak velocity. This leads to a strong density reduction in the upper layers and a corresponding increase of the field strength, together with the formation of a ‘Wilson depression’, i.e., a lowering of the level of optical depth unity within the flux concentration by about 300 km. This sequence of events, i.e., flux accumulation by converging horizontal flows, partial evacuation and field amplification by accelerated downflows, is in general agreement with the picture of flux expulsion followed



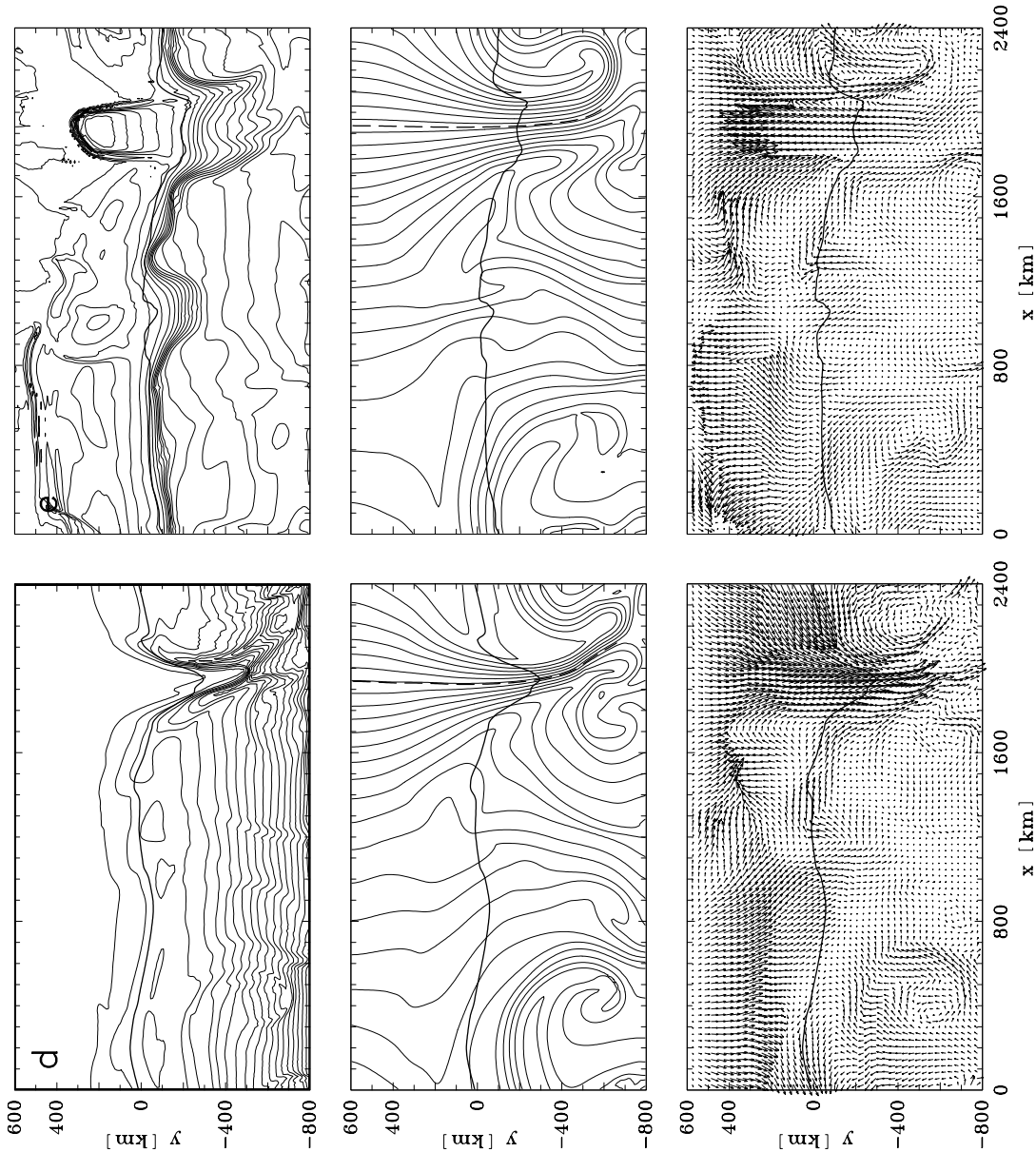


**Fig. 1a–e.** (see also opposite page) Formation of a magnetic flux sheet in run C4, starting from a homogeneous, vertical magnetic field of 400 G. Each snapshot consists of a column of three panels, showing density contours (top), magnetic field lines (middle), and velocity vectors (bottom), respectively. The columns **a** to **e** correspond to the times 0 s, 50 s, 100 s, 150 s, and 250 s, respectively. In the last snapshot the density panel is replaced by a plot of isothermals. The horizontally running thick curve indicates the optical depth  $\tau_5 = 1$ . The dashed curve shows the central field line of the flux sheet. Note that the boundary conditions at the sides of the box are periodic, so that field lines and flows leaving at one side re-enter through the other side.

by convective collapse. It takes only about 100 seconds for the strong flux accumulation to be formed.

As can be seen in snapshot (a) of Fig. 1a–e, the downflow has not yet reached the bottom of the computational box when the magnetic field is introduced, so that at a depth of about 600 km the strongly accelerated downflow within the flux sheet impinges on a fluid of much higher density. In fact, the matter descends so fast that it ‘piles up’ on top of this material as can be seen in the velocity field of snapshot (d) and in the corresponding density plot. This compression reverses the downflow into

an upflow and so prevents further intensification and downward extension of the flux sheet. The upflow develops into a shock wave, forming close to optical depth unity inside the flux concentration,  $y \simeq -300$  km. The temporal evolution of the vertical velocity is illustrated in Fig. 2, which shows height profiles along the central field line of the projected flux sheet (indicated by the dashed line in Fig. 1a–e). The downflow comes to a halt at the ‘bottom’ of the flux sheet and turns into an upflow, which rapidly develops a shock front. The speed of this front increases from  $\approx 8 \text{ km s}^{-1}$  at  $y = -250$  km to over  $17 \text{ km s}^{-1}$  when the

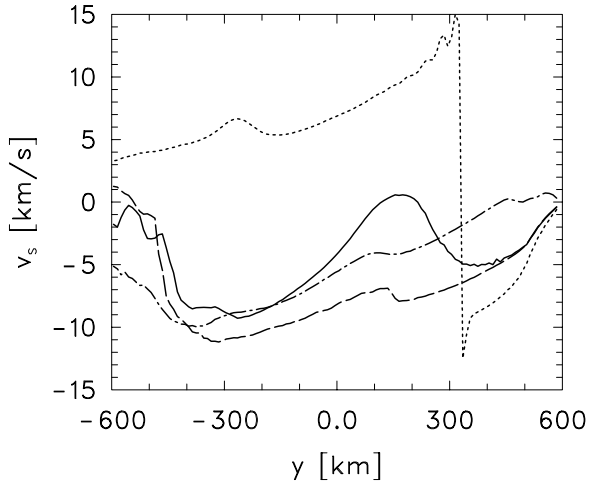


**Fig. 2.** Vertical velocity as a function of height along the central field line of the flux sheet (dashed line in Fig. 1a–e). Profiles are given at times  $t = 50$  s (solid),  $t = 100$  s (dot dashed),  $t = 150$  s (dashed), and  $t = 250$  s (dotted). These times correspond to the snapshots (b) to (e) of Fig. 1a–e.

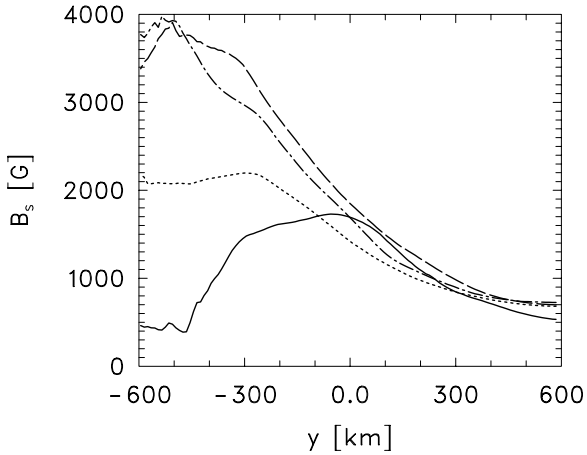


**Fig. 3.** Field strength as a function of height along the central field line of the flux sheet. The curves refer to the same times as in Fig. 2.

shock reaches a height of  $y = 430$  km. The shock front is well visible in the temperature plot at instant (e) of Fig. 1a–e, because a thin layer behind the front is 2600 K hotter than the ambient medium. The drop of the gas pressure across the shock front is about a factor 30. The upflowing gas leads to a dispersal of the magnetic flux (the reverse of the ‘convective collapse’) and the flux sheet dissolves at time  $t \approx 400$  s. This sequence of events is reminiscent to the scenario proposed by Schüssler (1990).

The temporal evolution of the field strength along the central field line is shown in Fig. 3 for the same moments as in Fig. 2. The field is strongly amplified in the course of the collapse and kilogauss field strength are rapidly reached. The ensuing upflow phase causes a dispersal of the field and a concomitant decline of the field strength (dotted line in Fig. 3). For a possible observational detection of the collapse process the magnetic field strength at given *optical* depth and the continuum intensity

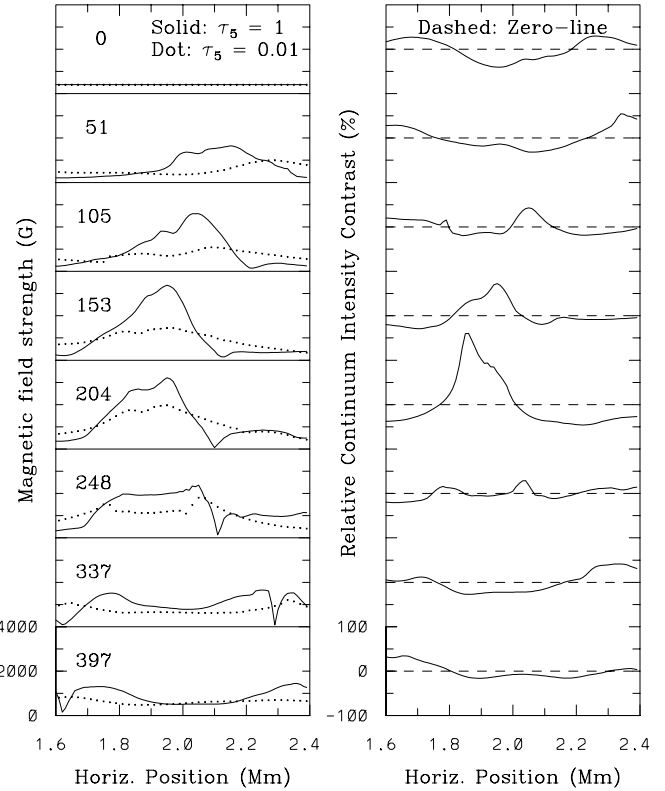


**Fig. 4.** Temporal evolution of the magnetic field strength at two continuum optical depths (left) and of continuum intensity contrast,  $(I(x) - \langle I \rangle) / \langle I \rangle$ , where  $\langle I \rangle$  is the horizontal average at 500 nm (right), both as functions of horizontal position ( $1600 \text{ km} \leq x \leq 2400 \text{ km}$ ). Times are given in seconds at the left-hand margin of the left column. The vertical scale, indicated at the bottom, is the same for every profile in a column.

contrast is of particular interest. The left-hand column of Fig. 4 shows the field strength for a number of moments in the time evolution as a function of the horizontal coordinate,  $1600 \text{ km} \leq x \leq 2400 \text{ km}$ , at two different optical depths (500 nm wavelength), namely  $\tau_5 = 1$  (continuum layer) and  $\tau_5 = 0.01$  (formation region of medium strong lines used for observational diagnostics), while the continuum intensity contrast is given in the right-hand column. Between 150 s and 200 s the field strength reaches its maximum value and, at the same time, the core of the flux sheet becomes very bright in the continuum. The contrast reaches 150% in a narrow peak of  $\approx 100$  km width while the field strength at  $\tau_5 = 0.01$  exceeds 1 kG in a region of about 400 km width. The subsequent dispersal and weakening of the field is accompanied by a corresponding decline of the intensity contrast, so that after a rather short interval of strong field and large contrast the region becomes inconspicuous in magnetic field and continuum brightness. On the other hand, magnetic flux contained in the flux sheet is steadily growing during the whole lifetime of the flux sheet. This is caused by the persistence of the horizontal convective flow towards the flux concentration, so that magnetic flux expulsion continues until the flux sheet finally dissolves (Steiner 1996).

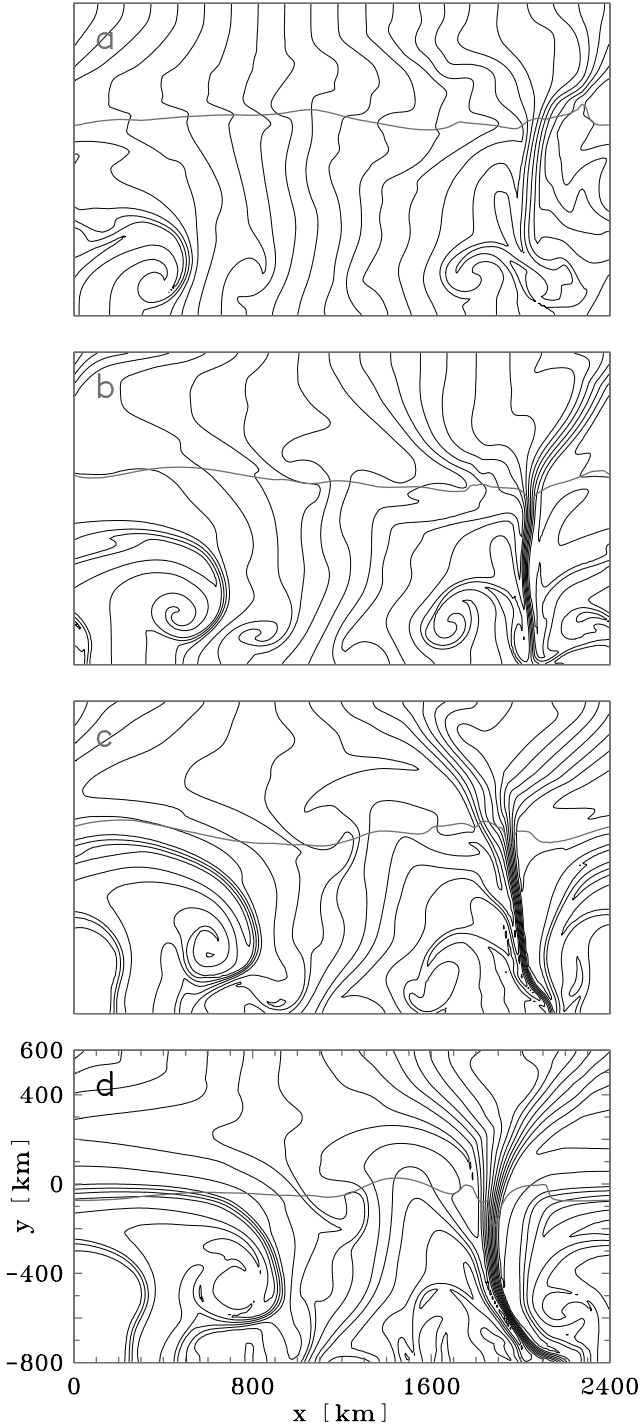


**Fig. 5a–d.** Time evolution of the magnetic field in run C1. The panels **a–d** give the instantaneous field line patterns at 60 s, 115 s, 175 s, and 230 s, respectively, after imposing an initially homogeneous magnetic field of 100 G. Note that after instant **b** the flux sheet extends through the (open) bottom of the computational domain.

Let us now turn to run C1. It starts from the same flow pattern as run C4 but has a weaker initial field strength of 100 G. Fig. 5a–d shows 4 moments of the time evolution of the magnetic field line pattern. The initial development is similar to run

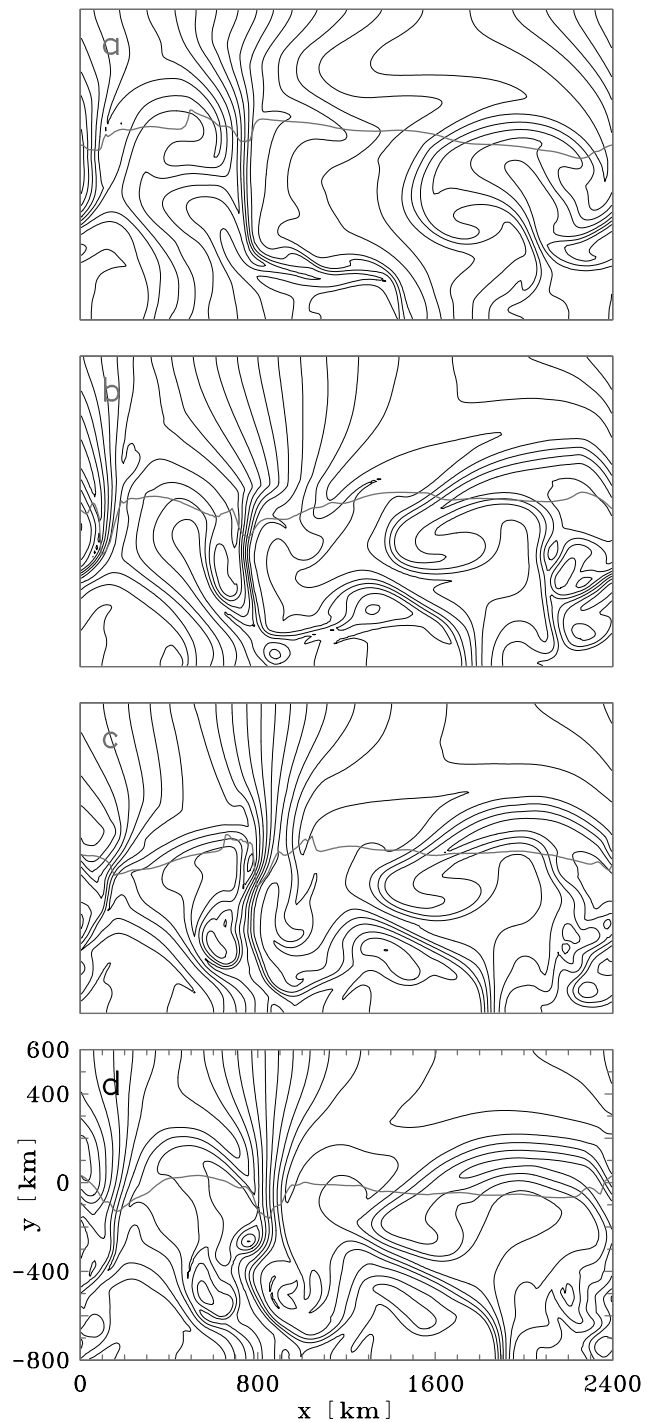


**Fig. 6a–d.** Time evolution of the magnetic field in run C2. The panels **a–d** give the instantaneous field line patterns at 100 s, 200 s, 250 s, and 300 s, respectively, after imposing an initially homogeneous magnetic field of 200 G. The initial convection pattern is different from that used in runs C1 and C4.

C4, a flux concentration forming at the site of the strong down-flow at  $x \simeq 2000$  km. Due to the smaller amount of magnetic flux in the box, the width of the flux sheet is much smaller and the dynamics of the convective pattern is less affected than in

the case of run C4. In particular, the downflow within the flux sheet is weaker so that no flow reversal with ensuing dispersal of the flux sheet takes place. The flux sheet extends through the (open) bottom of the computational box and persists throughout the simulation time of about 5 minutes. The lower efficiency of the collapse process as compared to run C4 is also reflected in the smaller maximum field strengths of  $\simeq 2000$  G at  $\tau_5 = 1$  and  $\simeq 1000$  G at  $\tau_5 = 0.1$ . The maximum continuum intensity contrast amounts to about 50%. These maxima are reached after about 3 min. Comparing Figs. 5a–d and 1a–e we find that the evolution of the overall pattern of field lines is very similar in both runs. The difference is mainly in the internal dynamics of the flux sheet: while the vigorous downflow in run C4 rebounds and eventually leads to the dissolution of the flux sheet, the thinner magnetic structure forming in run C1 is more efficiently heated by lateral influx of radiation, so that the downflowing gas becomes less dense and, therefore, less strongly accelerated. The evacuation of the upper layers is smaller in this case and, therefore, the efficiency of the convective collapse diminished (Venkatakrisnan 1986). The more gentle downflow does not rebound and smoothly continues through the lower boundary of the box, resulting in a persistent and vertically coherent magnetic structure within the computational domain.

The evolution of the magnetic field in run C2, starting with a different convection pattern and with an initial field of 200 G, is shown in Fig. 6a–d. We now have two strong downflows situated at  $x \simeq 100$  km and at  $x \simeq 800$  km, respectively, and magnetic flux concentrations form at both sites. The flux concentration at  $x \simeq 100$  km (near the left-hand margin of the panels) remains rather superficial since the corresponding downflow channel dissolves a few hundred km below  $y = 0$ . Nevertheless, field strengths of up to 2500 G ( $\tau_5 = 1.$ ) and 1500 G ( $\tau_5 = .01$ ) are reached. The flux sheet at  $x \simeq 800$  km extends to somewhat deeper layers and persists until the end of the simulation. The continuum contrast of this structure first becomes positive after about 100 seconds and from that time on the feature remains detectable as a bright structure with variable intensity. Contrast maxima of about 75% are reached after 2 and 4 minutes, respectively. The field strength reaches about the same values as for the other flux concentration. Similar to, but less vigorously than in run C4, the downflow within the flux sheet at  $x \simeq 800$  km becomes sufficiently strong to eventually reverse its direction and develop into an upward propagating shock. On the other hand, although the field weakens somewhat, the upflow is not so strong as to disperse the magnetic flux as rapidly as in run C4 and the field concentration persists throughout the whole simulation time of about 5 minutes.

Besides the formation of intense concentrations of vertical magnetic field we find in all simulations also strong *horizontal* fields above convective upflows (cf. Figs. 1a–e, 5a–d, 6a–d) with field strengths often exceeding 1000 G at optical depth unity. Although such features are certainly favored by our two-dimensional geometry, it is interesting to note that there seems to exist some observational evidence for rather strong horizontal fields in the quiet solar photosphere (Lites et al. 1996).

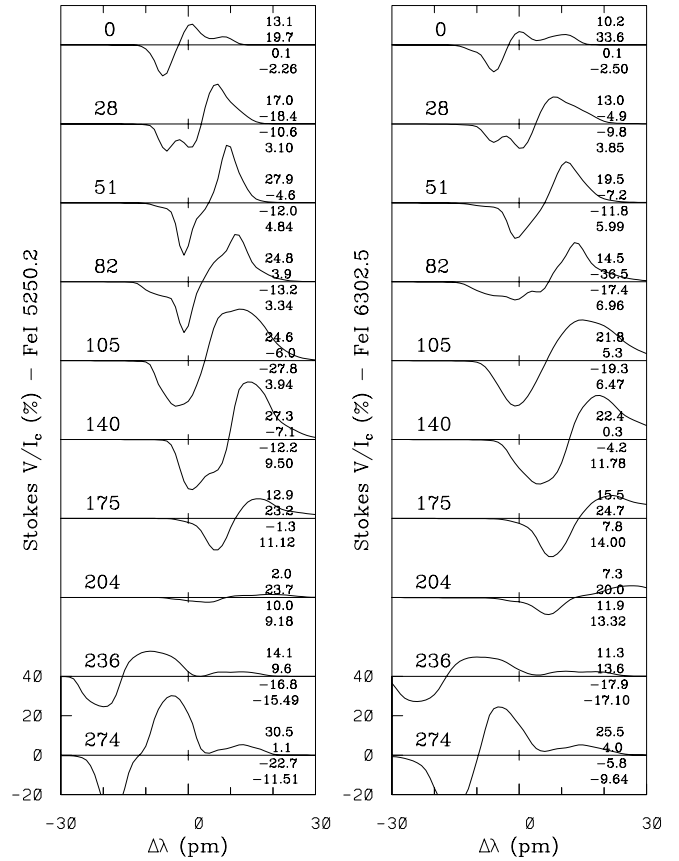


**Fig. 7.** Sequence of Stokes  $V$  profiles of the lines Fe I 525.02 nm and Fe I 630.25 nm covering the formation of the flux sheet and part of the ensuing upflow phase in run C4. The profiles are spatial averages over the range 1800–2200 km. The times (in seconds) are given at the left-hand side of each profile; at the right-hand side are printed (from top to bottom): mean amplitude (in percent of the continuum intensity), amplitude and area asymmetry (in percent), and shift of zero crossing (in pm). The vertical scale, indicated at the bottom, is the same for all profiles shown.  $\Delta\lambda = 0$  corresponds to the rest wavelength of the line center.

#### 4. Stokes diagnostics

Measurements of the continuum intensity and of the Stokes parameters of spectral lines with high spatial resolution could provide clues for the identification of a convective collapse process as it occurs in our simulations. In order to derive observables that could serve as signature for the simulated processes we computed the Stokes parameters of several spectral lines in the visible and infrared. These were obtained by integrating the transfer equation for polarized light along vertical rays placed equidistantly across the computational domain, typically at the grid resolution of 10 km. Averages over a number of rays were formed in order to compare with observations with finite spatial resolution. We found various characteristic features which would permit the identification of a convective collapse event. Since these signatures are clearest for the rather large flux sheet forming in run C4, we shall concentrate the discussion on that model.

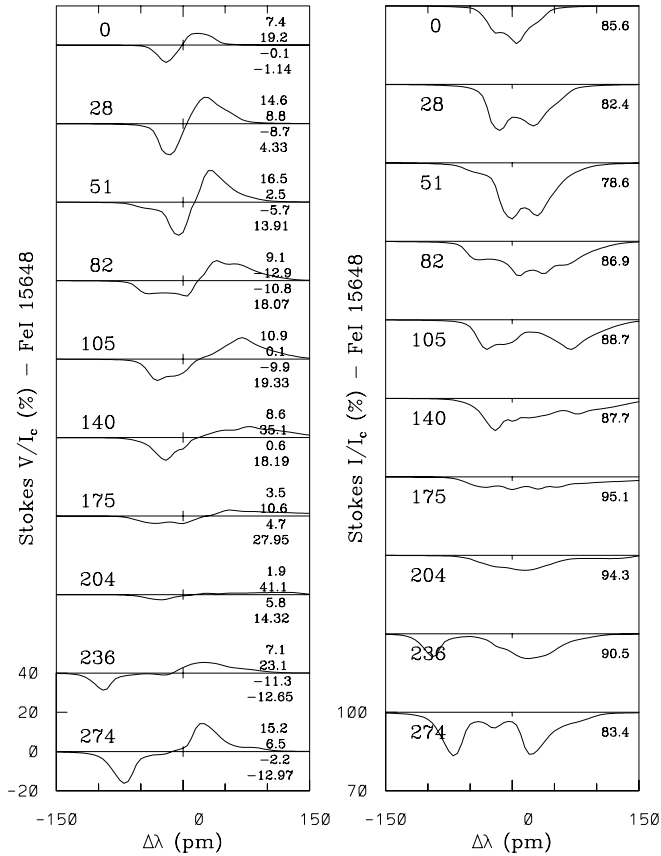


**Fig. 8.** Sequence of Stokes  $V$  (left) and Stokes  $I$  (right) profiles of Fe I 1.5648  $\mu\text{m}$  covering the same period of time as Fig. 7. The numbers at the right hand side of the Stokes  $I$  profiles represent the minimum intensity. The vertical scale, indicated at the bottom, is the same for all profiles in a column. All other notation is as in Fig. 7.

Let us begin with temporal sequences of Stokes  $I$  and  $V$  profiles, spatially averaged over the range 1800–2200 km, which is the region where the flux sheet forms. This corresponds to a spatial resolution of about  $0.5''$ . Fig. 7 shows Stokes  $V$  profiles of two visible spectral lines with large Landé factors, Fe I 525.02 nm ( $g_{\text{eff}} = 3$ ) and Fe I 630.25 nm ( $g_{\text{eff}} = 2.5$ ), while Fig. 8 gives Stokes  $V$  and  $I$  profiles of the infrared line Fe I 1.5648  $\mu\text{m}$  ( $g_{\text{eff}} = 3$ ). The evolution of the flow pattern is clearly recognizable in the wavelength shifts of the Stokes  $V$  profiles: A rapidly accelerating downflow followed by an even stronger upflow. In the short intervening period the Stokes  $V$  amplitudes become small. This phenomenon is obviously *not* due to magnetic flux disappearance but rather to both a partial cancellation of the Stokes  $V$  lobes owing to the presence of velocities of opposite signs and - even more important - an increased temperature with a flatter depth profile.

The flow signature of the convective collapse is most easily visualized in the shift of the zero crossing of Stokes  $V$  with respect to the rest wavelength of the line center. This shift, in terms of the corresponding Doppler velocity, is shown in Fig. 9 for the three spectral lines considered so far. Although the lines are formed in different parts of the atmosphere, the temporal

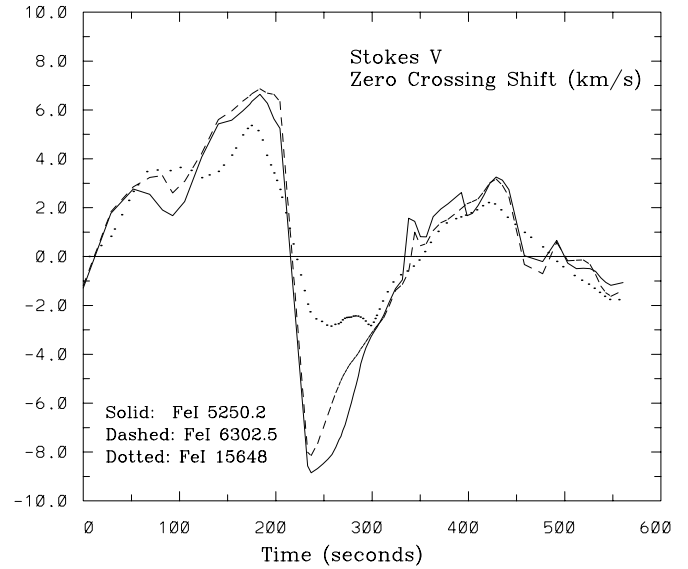


**Fig. 9.** Stokes  $V$  zero crossing shift, represented as Doppler velocity given in  $\text{km s}^{-1}$ , for the spectral lines, Fe I 525.02 nm, Fe I 630.25 nm, and Fe I 1.5648  $\mu\text{m}$  as a function of time for run C4. Positive shift indicates a downflow, negative shift an upflow.

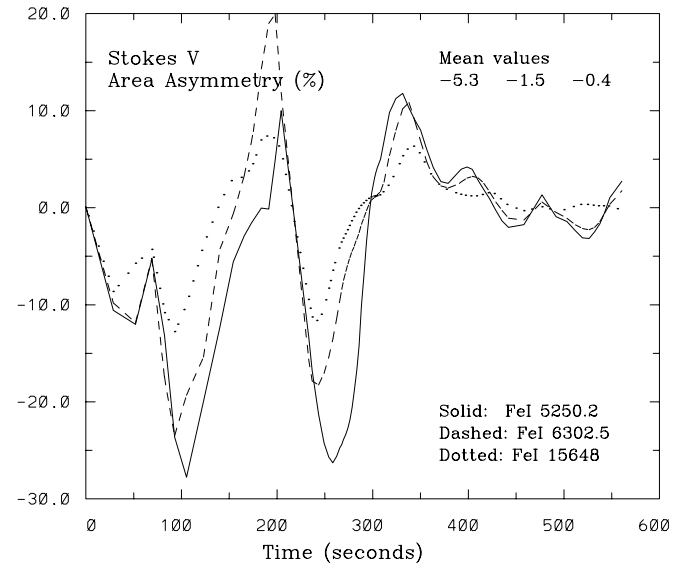


**Fig. 10.** Stokes  $V$  area asymmetry of the spectral lines Fe I 525.02 nm, Fe I 630.25 nm, and Fe I 1.5648  $\mu\text{m}$  as a function of time for run C4.

behaviour of the zero crossing shifts of their Stokes  $V$  profiles is almost identical: The unequivocal signature of a rapidly increasing downflow coming to an abrupt halt after about 200 sec, which is followed by an even stronger upflow.

More is to be learned about the structure of the velocity field of the convective collapse from the analysis of the Stokes  $V$  area asymmetry, a measure of the net circular polarization in the Stokes  $V$  profile, arising from the combined effect of magnetic field and velocity gradients (see Solanki 1993). Fig. 10 shows the area asymmetry of our three lines plotted as a function of time. It is seen that during both downflow- and upflow phases the area

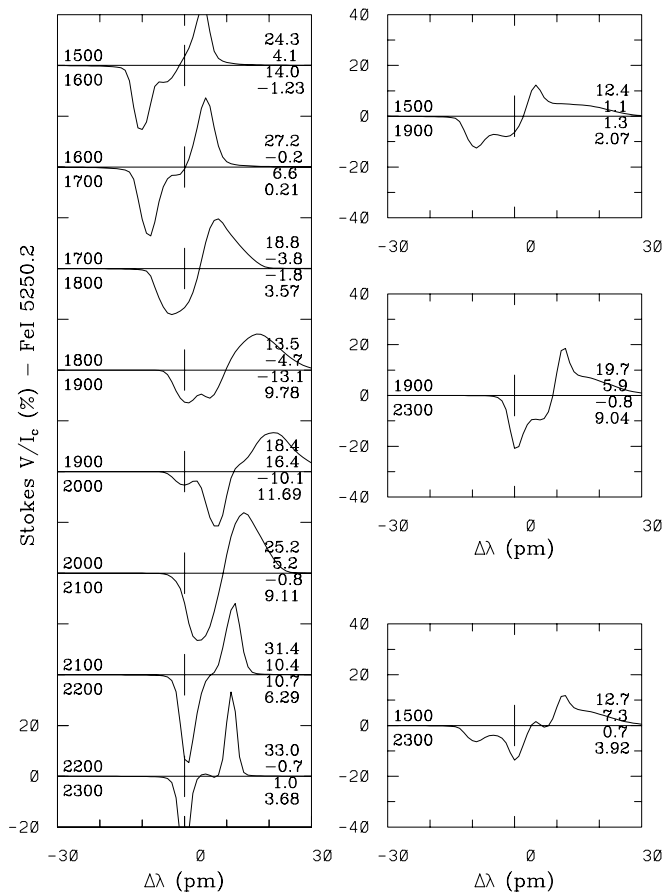


**Fig. 11.** Stokes  $V$  profiles of Fe I 525.02 nm at time  $t = 150$  s of run C4 (panel d in Fig. 1a–e), horizontally averaged over 100 km (left-hand column), 400 km (top and middle panel to the right), and 800 km (bottom panel to the right). The boundaries (in km) of the averaging intervals are indicated to the left of each panel. The remaining notation is as in Fig. 7.

asymmetry is strongly negative while in the short intervening interval it is slightly positive. The Stokes  $V$  area asymmetry becomes negative if the magnetic field strength increases with depth and the vertical flow speed increases in the direction of the velocity vector, i.e., a downflow whose speed increases with depth or an upflow whose speed increases with height (Solanki & Pahlke 1988). Such velocity gradients arise from the effect of the ambient superadiabatic stratification on a flow (Parker 1978).

While these sequences clearly reveal the signature of the dynamics, an unambiguous identification of the convective collapse requires information about the magnetic field intensification. The Zeeman splitting of lines in the visible is typically not larger than their Doppler width and, furthermore, the averaged Stokes  $V$  profiles often contain components with strongly different velocities, so that the distance between the peaks is no reliable diagnostic for the field strength, even for very strong fields. This problem is illustrated in Fig. 11, showing Stokes  $V$  profiles of Fe I 525.02 nm at time  $t = 150$  s (panel d in Fig. 1a–e) for various horizontal averaging intervals corresponding to a spatial

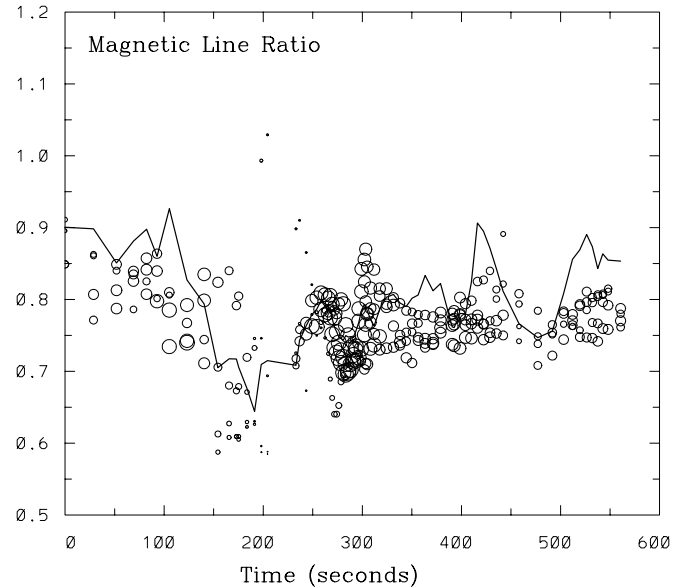


**Fig. 12.** ‘Magnetic line ratio’ (MLR) of Fe I 525.02 nm and Fe I 524.71 nm, as a function of time for run C4. The solid line represents the values derived from the spatial averages over the range 1800–2200 km, while the circles represent 100 km averages (1800–1900, 1900–2000, 2000–2100 and 2100–2200 km). The diameter of a circle is proportional to the corresponding mean Stokes  $V$  amplitude.

resolution of about  $0.1''$ ,  $0.5''$ , and  $1''$ , respectively. The spatially variable line-of-sight velocity leads to complicated composite  $V$  profiles unless a very high spatial resolution is achieved.

More reliable information about the magnetic field evolution can be obtained from the infrared line Fe I  $1.5648 \mu\text{m}$ . Since the Zeeman splitting varies as  $\lambda^2$ , this line is completely split in the presence of the prevailing field, as can be seen in Fig. 8. Hence, the separation of the peaks of both Stokes  $I$  and Stokes  $V$  allows us to determine the magnetic field strength with reasonable accuracy. We obtain a field strength of about 600 G at 28 sec, which increases to about 1500 G 80 sec later – this is at about the peak of the field intensification. Thereafter the profiles become rather distorted which prevents a reliable field strength determination. At 270 sec a neat profile reappears from which we obtain 1300 G. These results are in good agreement with the values given in Fig. 4.

Another method to check whether a field intensification to kilogauss values has taken place is to determine the ‘magnetic line ratio’ (MLR), which is defined as the ratio of the Stokes  $V$  amplitudes of the lines Fe I 525.02 nm and Fe I 524.71 nm, divided by their respective Landé factors (Stenflo 1973). The MLR is fairly insensitive to temperature variations (the energy of the lower level of the two lines is nearly identical) but it is a – not very strong – function of the magnetic field strength, decreasing from unity for weak fields to about 0.65 for fields of about 1500 G or more. The MLR is thus not very useful for the exact determination of the strength of a given magnetic field. However, if the MLR is found to have assumed a value around 0.8 or below it is safe to conclude that a kilogauss field

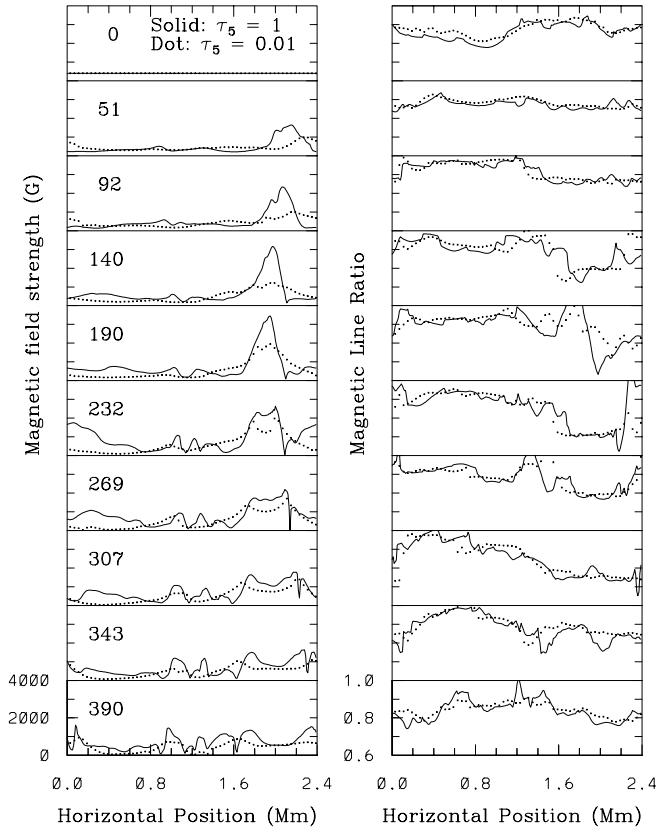


**Fig. 13.** Temporal sequences of magnetic field strength (left column) and MLR (right column) of run C4 as a function of horizontal position. In the left-hand panels the solid line represents the magnetic field strength at  $\tau_5 = 1$ , the dotted line at  $\tau_5 = 0.01$ ; the numbers in the left-hand panels indicate the time in seconds. The MLR in the right-hand panels is shown with  $0.5''$  (solid lines) and  $1''$  (dotted lines) spatial resolution. The vertical scale, indicated at the bottom, is the same for all curves in a column.

is present at that location. In particular, the temporal evolution of the MLR from a value around unity to values below 0.7 is the unambiguous signature of a significant field enhancement. The MLR as a function of time is given in Fig. 12. The solid line represents our usual spatial average over the range 1800–2200 km. In order to show the dependence of the MLR on the spatial resolution, the circles denote MLR values derived from averages over 100 km in the same bracket, i.e., 1800–1900, 1900–2000 km, etc.; the diameter of the circles is proportional to the respective Stokes  $V$  amplitudes. The plot clearly reveals the strong field enhancement during the downflow phase (cf. Fig. 2). The field strength appears to reach its maximum value in the intermediate phase when the dominant velocity is changing sign and the amplitudes of the Stokes parameters become very small – which is essentially in agreement with the actual evolution of the field strength as shown in Fig. 4. The decay of the field after the onset of the upflow is also indicated. On the other hand, the rather strong variation of the MLR for higher spatial resolution suggests that a reasonable precise measurement of the field strength is difficult to obtain from the MLR alone.

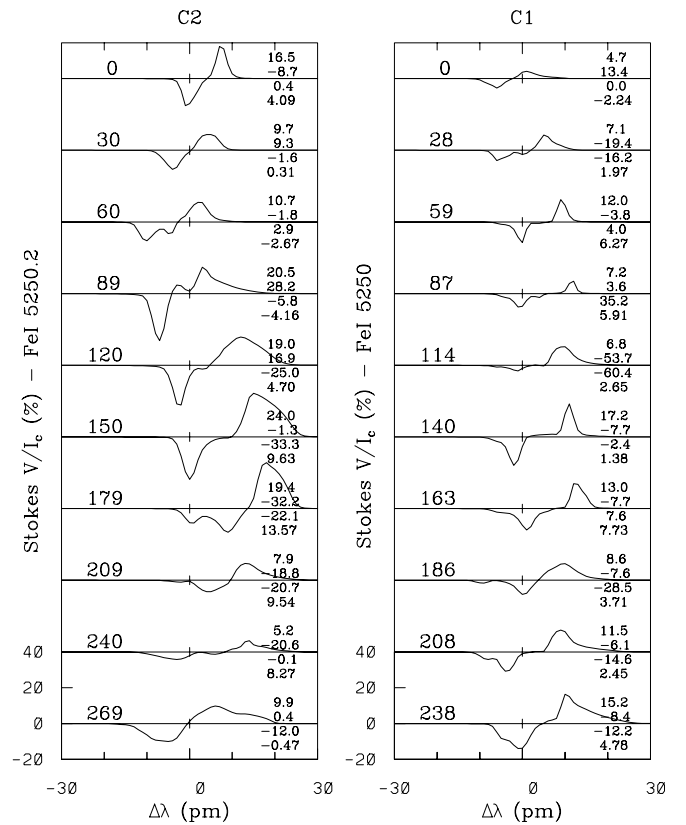


**Fig. 14.** Temporal sequences of Stokes  $V$  of Fe I 525.02 nm for run C2 (left) and for run C1 (right). The profiles represent spatial averages over 600–1000 km (model C2) and 1750–2150 km (model C1). All other notation is as in Fig. 7.

Further clues for the significance of spatial resolution when collecting data for the determination of the MLR may be obtained from Fig. 13 which gives, for ten consecutive snapshots, the MLR as a function of  $x$  at a spatial resolution of roughly  $0.5''$  and  $1''$  (400 km and 800 km), respectively, together with the horizontal profiles of the magnetic field strength at two optical depths. The full horizontal extension of the computational domain is shown. It is seen that during the period of about 170 sec after start of the collapse until about 100 sec later the MLR assumes low values that are clearly indicative of strong fields in the range around  $x = 2000$  km where the flux sheet has formed. The MLR dip can be identified at both spatial resolutions although at  $0.5''$  this may be somewhat easier.

As already discussed in the previous section, the downflow and the convective intensification of the magnetic field are weaker in the models C1 and C2. The dynamic signatures of the convective collapse (redshifted zero crossing and negative area asymmetry of the Stokes  $V$ -profiles) are clearly visible in Fig. 14, which shows temporal sequences of Stokes  $V$  profiles of the line Fe I 525.02 nm, averaged over 400 km in both cases. Upflows and shocks in the higher layers disturb the profiles in the early phases of the simulations, but the collapse signature becomes dominant after about 2 minutes for model C2 (left column) and after 1 minute for model C1 (right column). The

intensification of the magnetic field to kilogauss values, however, is much harder to detect: the flux sheets are much narrower and the magnetic field is weaker than in the case of model C4, so that it requires a spatial resolution of about 100 km in order to detect a clear signature in the MLR.

## 5. Discussion

The three examples presented here display a variety of behavior, depending on the amount of magnetic flux accumulated in a flux concentration. While the comparatively wide flux sheet in run C4 is dispersed after only a few minutes due to a strong upflow (the inverse of the convective collapse), the narrower flux concentrations forming in runs C1 and C2 show only mild, if any, upflows and last longer. Their downflows are weaker and hence the collapse process is less efficient in these cases, leading to smaller (but still kilogauss) field strengths. A decreasing efficiency of the convective collapse with diminishing size of the flux concentration has been predicted by Venkatakrisnan (1986), who considered the effect of radiative energy exchange between a flux tube and the external gas, reducing the effect of the external superadiabaticity. This may also contribute to explaining the departure of our results from the prediction of Spruit (1979) that the final field strength (after the collapse) should decrease with increasing initial field strength (decreasing initial value of  $\beta$ ). Spruit assumed as initial state a thin flux tube in temperature equilibrium with the exterior and did not include radiative energy exchange.

The conspicuous upflow in run C4 may be of some interest with regard to the origin of spicules. The flow develops an upward traveling shock front, which may be sufficiently strong to lift chromospheric matter to coronal heights and produce a spicule by mechanisms similar to those described by Sterling & Hollweg (1988). When the shock front forms at  $\tau_5 \simeq 1$ , the flux concentration is already in the course of dissolving. By the time ( $\gtrsim 100$  s) the shock front reaches chromospheric layers or the transition region the flux concentration is likely to have completely dissolved, so that a one-to-one correspondence between photospheric flux concentrations and spicules would not be expected if spicules indeed originate in that way.

Let us briefly comment on the limitations of the present work. Although we expect elongated structures similar to flux sheets to form in intergranular lanes if a sufficient amount of magnetic flux is available, our 2D simulations give only a restricted view of the evolution possible in the real 3D world. However, the basic physical processes like flux expulsion, downflow acceleration, and field intensification are fully present in 2D and we do not expect fundamental differences arising in a 3D simulation (cf. Nordlund & Stein 1989).

## 6. Conclusion

We have simulated the formation of intense magnetic flux sheets in the uppermost layers of the solar convection zone and the photosphere. The two-dimensional geometry of our simulations allowed us, for the first time, to study the crucial interplay be-

tween the processes of flux expulsion and convective collapse with high spatial resolution of the numerical grid. Previous simulations were either based on the (1D) thin-flux-tube approximation and ignored the convective flows or, in the 3D case, they were limited to coarse spatial resolution.

The basic predictions from numerical experiments of flux expulsion and linear analysis of the convective collapse process are confirmed by our results: magnetic flux is rapidly swept into the convective downflow regions and the upper parts of the forming flux concentrations are partially evacuated by a vigorous downflow along the magnetic field, leading to an intensification of the field up to the observed kilogauss values. The superadiabatic (mean) stratification and the radiative cooling of the gas lead to a forceful acceleration of the downflow.

The structure and evolution of such a flux concentration depends significantly on the amount of magnetic flux it contains and also on the convective flow pattern at the time of its formation. In the case of a thick flux sheet, upflows with shocks can be driven by the ‘rebound’ of the very strong downflow from the high-density material in the deeper layers. Such an upflow may destroy the flux sheet a few minutes after its formation. Thin flux sheets host more gentle downflows and may persist for a longer time ( $> 5$  minutes) and also extend to deeper layers below the visible surface.

Observations in polarized light in the visible and infrared spectral regions may reveal the signatures of the simulated processes in the photosphere of the Sun. The combination of a redshift with a negative area asymmetry of Stokes  $V$  profiles indicates an accelerated downflow, while the intensification of the field may be detected by the magnetic line ratio technique and the direct Zeeman splitting of spectral lines in the infrared. For the thicker flux sheet a spatial resolution of  $0.5''$  may suffice, but for the smaller flux concentrations a value around  $0.1''$  is required in order to reliably establish the process of convective collapse by observational means.

*Acknowledgements.* This work has been supported by the DFG (Deutsche Forschungsgemeinschaft) under grant Schu 500/6.

## References

- Chan K.L., Sofia S., 1986, ApJ 307, 222
- Galloway D.J., Proctor M.R.E., Weiss N.O., 1977, Nat 266, 686
- Hasan S.S., 1984, ApJ 285, 851
- Hasan S.S., 1985, AA 143, 39
- Hossain M., Mullan D.J., 1993, ApJ 416, 733
- Lites B.W., Leka K.D., Skumanich A., Martínez Pillet V., Shimizu T., 1996, ApJ 460, 1019
- Nordlund Å, 1986, in: Small-scale Magnetic Flux Concentrations in the Solar Photosphere, eds. W. Deinzer, M. Knölker, H.H. Voigt, Abh. d. Akad. d. Wiss. Göttingen 38, p. 83 (ISBN 3-525-82113-1)
- Nordlund Å, Galsgaard K., Stein R.F., 1994, in: Solar Surface Magnetism, eds. R.J. Rutten, C.J. Schrijver, Kluwer, Dordrecht, p. 471
- Nordlund Å, Stein R.F., 1989, in: Solar and Stellar Granulation, eds. R.J. Rutten, G. Severino, Kluwer, Dordrecht, p. 453
- Nordlund Å, Stein R.F., 1990, Computer Phys. Comm., 59, 119
- Oran E.S., Boris J.P., 1987, Numerical Simulation of Reactive Flow, Elsevier, New York

- Parker E.N., 1963, *ApJ* 138, 552  
Parker E.N., 1978, *ApJ* 221, 368  
Parker E.N., 1979, *Cosmical Magnetic Fields*, Clarendon, Oxford, Ch. 10  
Sato T., Hayashi T., 1979, *Phys. Fluids* 22, 1189  
Schüssler M., 1990, in: *Solar Photosphere: Structure, Convection, Magnetic Fields*, ed. J. O. Stenflo, IAU Symp. 138, Kluwer, Dordrecht, p. 161  
Solanki S.K., 1993, *Space Sci. Rev.* 63, 1  
Solanki S.K., Pahlke K.-D., 1988, *AA* 201, 143  
Spruit H.C., 1977, Ph.D. thesis, University of Utrecht  
Spruit H.C., 1979, *Sol. Phys.* 61, 363  
Spruit H.C., Zweibel E.G., 1979, *Sol. Phys.* 62, 15  
Steiner O., 1996, in: *Solar and Galactic Magnetic Fields*, eds. D. Schmitt, H.-H. Voigt, *Nachr. Akad. d. Wiss. Göttingen* 4/1996, Vandenhoeck & Ruprecht, p. 185  
Steiner O., Knölker M., Schüssler M., 1994, in: *Solar Surface Magnetism*, eds. R.J. Rutten, C.J. Schrijver, Kluwer, Dordrecht, p. 441  
Steiner O., Grossmann-Doerth U., Knölker M., Schüssler M., 1996, *Sol. Phys.* 164, 223  
Steiner O., Grossmann-Doerth U., Knölker M., Schüssler M., 1998, *ApJ* 495, 468  
Stenflo J.O., 1973, *Sol. Phys.* 32, 41  
Sterling A.C., Hollweg J.V., 1988, *ApJ* 327, 950  
Takeuchi A., 1993, *PASJ* 45, 811  
Takeuchi A., 1995, *PASJ* 47, 331  
Unno W., Ando H., 1979, *Geophys. Astrophys. Fluid Dyn.* 12, 107  
Venkatakrishnan P., 1983, *J. Astrophys. Astr.* 4, 135  
Venkatakrishnan P., 1985, *J. Astrophys. Astr.* 6, 21  
Venkatakrishnan P., 1986, *Nat* 322, 156  
Webb A.R., Roberts B., 1978, *Sol. Phys.* 59, 249  
Weiss N.O., 1966, *Proc. Roy. Soc. Lon. A* 293, 310